# A numerical and experimental hybrid approach for the investigation of aerodynamic forces on stay cables suffering from rain-wind induced vibration

Hui Li[a],*, Wen-Li Chen[a], Feng Xu[a], Feng-Chen Li[b], Jin-Ping Ou[a,c]

[a]*School of Civil Engineering, Harbin Institute of Technology, Harbin 150090, China*
[b]*School of Energy Science and Engineering, Harbin Institute of Technology, Harbin 150001, China*
[c]*School of Civil and Hydraulic Engineering, Dalian University of Technology, Dalian116024, China*

## Abstract

The aerodynamic forces on a stay cable under a rain-wind induced vibration (RWIV) are difficult to measure directly in a wind tunnel test. This paper presents a hybrid approach that combines an experiment with computational fluid dynamics (CFD) for the investigation on aerodynamic forces of a stay cable under a RWIV. The stay cable and flow field were considered as two substructures of the system. The oscillation of the stay cable was first measured by using a wind tunnel test of a RWIV under an artificial rainfall condition. The oscillation of the cable was treated as a previously known moving boundary condition and applied to the flow field. Only the flow field with the known moving cable boundary was then numerically simulated by using a CFD method (such as Fluent 6.3). The transient aerodynamic forces of the stay cable with a predetermined cable oscillation were obtained from numerical calculations. The characteristics of the aerodynamic forces in the time domain and frequency domain were then analysed for various cases. To verify the feasibility and accuracy of the proposed hybrid approach, the transient aerodynamic forces were applied to a single-degree-of-freedom model (SDOF) of the stay cable to calculate the RWIV of the cable. A comparison was performed between the oscillation responses of the stay cable obtained from the calculated (SDOF model) and experimental results, and the results indicate that the hybrid approach accurately simulates the transient aerodynamic forces of the stay cable. The equivalent damping ratios induced by the aerodynamic forces were obtained for various wind speeds. Furthermore, a nonlinear model of the aerodynamic force is proposed based on the calculation results, and the coefficients in the model were identified by a nonlinear least-squares technique.
© 2010 Elsevier Ltd. All rights reserved.

*Keywords:* Rain-wind induced vibration; Hybrid approach; Computational fluid dynamics (CFD); Stay cable; Aerodynamic force

## 1. Introduction

Long-span cable-stayed bridges have been constructed throughout the world due to their superior structural performance and elegant appearance. The inclined cables are key components of the cable-stayed bridges and are prone

*Corresponding author. Tel./fax: +86 451 86282013.
*E-mail address:* lihui@hit.edu.cn (H. Li).

to vibrate under wind, rain and traffic loads. A rain-wind induced vibration (RWIV) occurs if rain and wind act simultaneously on the inclined cables, which was first reported by Hikami and Shiraishi (1988) for the Meikonishi Bridge and then observed worldwide in other bridges. The rivulet is a key factor for the occurrence of the RWIV, and Robertson et al. (2010) performed a numerical simulation of rivulet evolution on a horizontal cable subject to an external aerodynamic field. Many wind tunnel experiments (Hikami and Shiraishi, 1988; Matsumoto et al., 1990, 1992, 1995, 1998, 2003; Flamand, 1995; Bosdogianni and Olivari, 1996; Verwiebe and Rucheweyh, 1998; Gu and Du, 2005; Cosentino et al., 2003; Li et al., 2010) have been performed to investigate this vibration. The wind tunnel experiments can reproduce the rain-wind induced vibrations of the cable segment models under the artificial rainfall conditions, and the vibration response of models can be obtained, but the flow fields around the vibrating cable models are not easily measured. Therefore, the simultaneous wind pressure and aerodynamic force cannot be directly obtained from a wind tunnel test.

CFD numerical simulation provides a tool to investigate the flow field of complex wind-induced vibration problems. For CFD numerical simulations, various numerical turbulent models that describe a turbulent flow field have been employed, including direct numerical simulation (DNS), discrete vortex method (DVM), Reynolds-averaged Navier–Stokes (RANS), large-eddy simulation (LES) and some combinations of them. Direct numerical simulation is the only method that is capable of capturing all of the aspects of the turbulence characteristics. However, modern computational hardware is not powerful enough to perform a DNS for a high Reynolds number (Re) turbulent flow, which occurs more frequently in reality. Dong and Karniadakis (2005) investigated turbulent flows past a rigid cylinder undergoing forced oscillations at Re = 10 000 by adopting a DNS method with a multilevel-type parallel algorithm. The parallel performance was demonstrated used a Compaq Alpha Cluster with 1536 processors for cylinder flow at Re = 10 000 with 300 000 000 degrees of freedom. The precision of the LES and RANS was less than the DNS but used much less computational time.

Although the required computational time and resources using other turbulent models are less than the DNS simulation for the fluid–solid interaction of structures, the structural finite element computation and the data transmission between the flow field and the finite element computation at each time step will require additional time compared to only the CFD numerical simulation of the flow field around the structures. This is especially true for long-span cables or complex bridge structures, which contain much more elements and degrees of freedom.

Structural response can be easily measured in wind tunnel experiments or in practical engineering, whereas the flow field around the structures is more difficult to obtain, especially for the RWIV of a stay cable. Based on this background, this paper presents a hybrid approach that combines an experiment with a CFD numerical simulation. The structure and the flow field are considered as two substructures of a system. The structural vibration measured from wind tunnel tests is considered as a known cable boundary condition and is applied to the flow field. Only the flow field with the previously known moving cable boundary was numerically simulated by using the Fluent 6.3 code. This hybrid approach is different from force oscillation tests in the wind tunnel (Koopman, 1967; Griffin and Votaw, 1972; Griffin and Ramberg, 1974). Independent control of the amplitude and frequency of the cylinder oscillations allows for an easier observation of the effects of varying either parameter. However, Parkinson (1989) claimed that the data cannot represent all of the characteristics of a fully coupled fluid–solid interaction problem, because the experiments are not designed to receive feedback from the flow field and the oscillation of the structure is not excited by the flow. An alternative solution is to experimentally simulate the fluid–solid interaction problem directly, and the oscillation of the structure is then excited by the flow field. The hybrid approach of tests combined with CFD not only solves the problem of measuring the flow field around the moving structures but also improves upon the experimental investigations of the forced oscillation tests because the structure motion was obtained from a wind tunnel test of a fully coupled fluid–solid interaction and was not separately appointed. Compared to the fluid–solid method of the CFD numerical simulation, the hybrid approach has some advantages. First, because the structural oscillation was accurately measured and the computational errors of the structural vibrations are absent (which will decrease the errors of the flow field simulation caused by the simulation of the structural vibrations), the CFD numerical simulation of the flow field around the oscillating structure may be of a higher precision. Second, the hybrid approach may reduce the computational time that is required for the finite element computations of the structure as well as the data transmission between the flow field and the finite element computations at each time step.

In this paper, the hybrid approach of tests combined with CFD is presented for the RWIV of a stay cable. The stay cable and the flow field are considered as two substructures of a system. The oscillation of the stay cable was measured by using a wind tunnel test of the RWIV under an artificial rainfall condition and was regarded as a known moving boundary condition and applied to the flow field through user-defined functions (UDFs) embedded in Fluent 6.3. Only the flow field with the previously measured moving boundary was numerically simulated by the Fluent CFD code, and the aerodynamic forces of the stay cable were then obtained by integrating the pressure on the cable surface. Because the measured vibrations of the cable and rivulet were accounted for in the flow-field model, the computational efficiency should be higher and the computational accuracy should improve.

The structure of this paper is organized as follows: in Section 2, the hybrid approach is introduced, and a comparison of the vortex-induced vibration of a cylinder is performed to verify the feasibility, computational efficiency and accuracy of the proposed hybrid approach. In Section 3, the hybrid method is used to obtain the aerodynamic forces on the stay cable model under a RWIV. In Section 4, the transient aerodynamic forces are analysed. The aerodynamic forces are applied to a single-degree-of-freedom model (SDOF) of the stay cable to calculate the oscillation response of the cable model. A comparison is performed between the oscillation response of the stay cable obtained from the calculation (SDOF model) and the experiment. The aerodynamic damping ratios of the stay cable are then evaluated at various wind speeds. Furthermore, a nonlinear aerodynamic force model is proposed, and the coefficients for the model are identified by using a nonlinear least-squares technique. Discussion of the hybrid method is given in Section 5 and is followed by the conclusion.

## 2. Method validation

To verify the feasibility, computational efficiency and accuracy of the proposed hybrid approach, the vortex-induced vibrations (VIV) of a cylinder using the common fluid–structure interaction (CFSI) approach was compared to the proposed hybrid approach.

The VIV of the cylinder was first computed using the common fluid–structure interaction (CFSI) method by using Fluent 6.3. A program created by the authors to calculate the cable vibration was integrated into the Fluent code. The oscillations of the cylinder and the aerodynamic forces on the cylinder surface were obtained by using the CFSI, and, as a reference. The calculated response of the cylinder was also considered as a previously known moving boundary if the behaviour of flow field was computed using the hybrid approach. For the hybrid approach, only the behaviour of the flow field with the specified moving boundary (obtained by the CFSI above) at the interface of the cylinder was simulated by Fluent 6.3, and the moving boundary was added at each time step. The aerodynamic forces on the surface of the cylinder were obtained by integrating the pressure at the interface of the flow field and the cable and were applied to the cylinder to calculate its VIV. The aerodynamic forces and VIV of the cylinder that resulted from these two procedures were compared.

Fig. 1 shows the computational domain and grid partitioning of the cable model. The rectangular computational region is $50D \times 20D$ ($D$ is the diameter of the cylinder), the upstream region is $10D$, the downstream region is $40D$ and the distance between the centre of the cylinder and the upper boundary (or lower boundary) of the computation domain is $10D$. The diameter of the cylinder is $D = 0.01$ m. The boundary conditions were defined as follows: the left side is the "velocity inlet" and the flow velocity is uniform; the right side is the "outflow" and is a fully developed outlet boundary; the upper and lower boundaries are "symmetry"; and the cylinder surface is the "wall". The SST $k-\omega$ turbulent model based on the RANS method was used to simulate the flow in the CFD numerical simulation. The fluid velocity of the cylinder surface was equal to the cylinder velocity, which was assigned by the UDFs.

The cylinder was elastically supported, and the cylinder vibrations were simplified as a mass-spring-damping system in which the CFSI was employed to investigate the VIV of the cylinder. $M$, $K$ and $C$ are the mass, stiffness and damping coefficients per unit length of the cylinder or the cable, respectively, $f_{cyl}$ is the natural frequency of the cylinder and $f_{vox}$ is the vortex shedding frequency of flow around the same static cylinder. The numerical simulation of the vortex-induced vibration of the cylinder was performed at Re = 200. The time step size was set as 0.002 s, and the wind speed was maintained at 0.2921 m/s for which $f_{vox}$ is equal to 5.52 Hz. Unstructured triangular meshes were used to partition the flow field, and the number of grid cells was about 30 000.

The cylinder oscillation response, which was solved by using the Newmark–β method, and the aerodynamic coefficients at frequency ratios $f_{cyl}/f_{vox}$ of 1.04 and 1.15 were calculated using the CFSI method in Fluent and
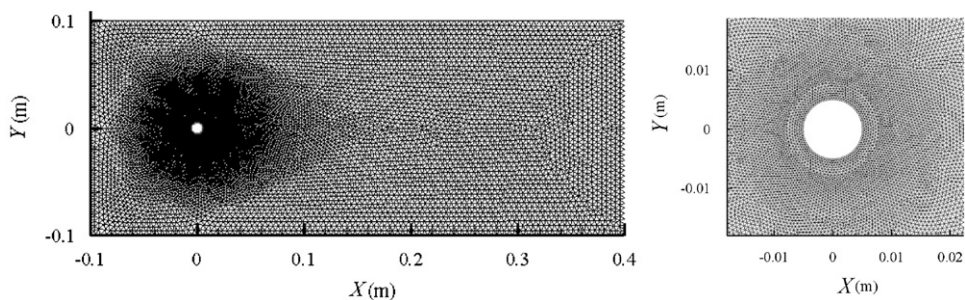


Fig. 1. Computational domain and grid partitioning.

embedding a UDF that could solve the cylinder oscillation and capture the mesh moving in the flow field as shown in Figs. 2 and 3, respectively.

To calculate the VIV of the cylinder using the proposed hybrid approach, the cylinder oscillations shown in Figs. 2(a) and (b) were added as the movement of the cylinder boundary by using UDFs for frequency ratios of 1.04 and 1.15, respectively. The flow field around the moving boundary was numerically simulated by using Fluent. The same computational domain, grid number, time step and cylinder parameters were used as they were in the CFSI method. The aerodynamic coefficients that were obtained using these two approaches were then compared. The lift coefficient $C_y$ and drag coefficient $C_x$ obtained by using the CFSI method and the hybrid approach are denoted as $C_{yC}$, $C_{xC}$ and $C_{yH}$, $C_{xH}$, respectively. Figs. 4 and 5 show a comparison of the aerodynamic coefficients at frequency ratios of 1.04 and 1.15, respectively. The comparison indicates that the lift coefficients $C_{yC}$ and $C_{yH}$ were similar to each other. A small difference is observed and can be attributed to the numerical simulation procedures (one focuses on only the flow field, while the other accounts for the flow field, cylinder and data transmission between the cylinder and flow field). The same conclusion can be made for the drag coefficients $C_{xC}$ and $C_{xH}$.

The aerodynamic force $F_{yH}$ that was calculated through the proposed hybrid method was added to the cylinder for external excitation. Consequently, the response of the cylinder can be obtained through the SDOF model of the cylinder using the following equation:

$$M\ddot{y} + C\dot{y} + Ky = F_y, \quad F_y = \tfrac{1}{2}\rho U^2 D C_y, \tag{1}$$

where $F_y$ and $C_y$ denote $F_{yH}$ and $C_{yH}$ as calculated by the proposed hybrid method, respectively; $\rho$ is the air density and was assumed to be 1.225 kg/m³; and $U$ is the velocity at the inlet. In this paper, Eq. (1) will also be used to analyse the RWIV response of the stay cable.
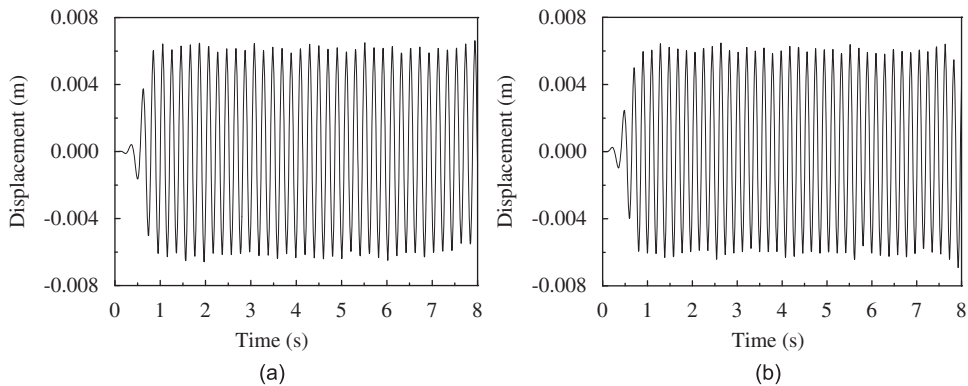


Fig. 2. Time histories of the cross-flow displacement of the cylinders for two frequency ratios: (a) 1.04 and (b) 1.15.
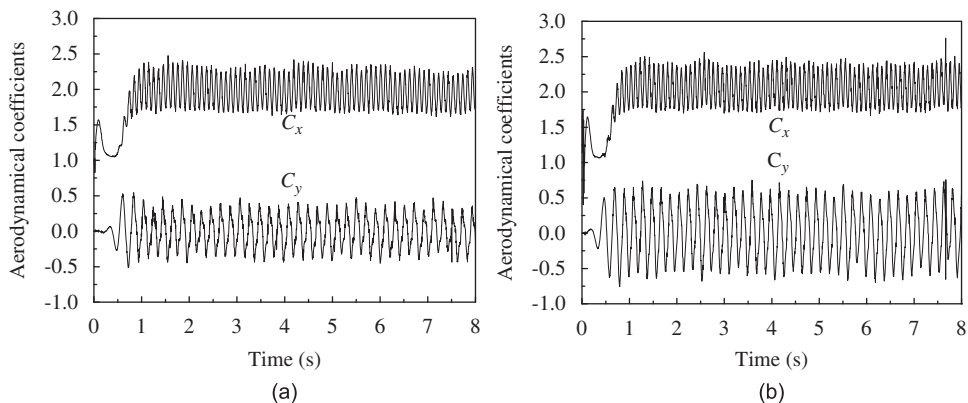


Fig. 3. Time histories of the aerodynamic coefficients for two frequency ratios: (a) 1.04 and (b) 1.15.
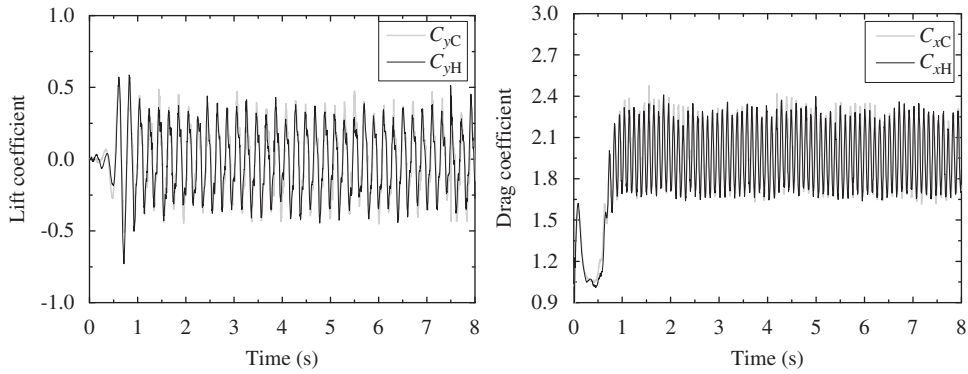
Fig. 4. Comparison of the aerodynamic coefficients obtained from the two numerical methods for a frequency ratio of 1.04: (a) lift coefficient and (b) drag coefficient.
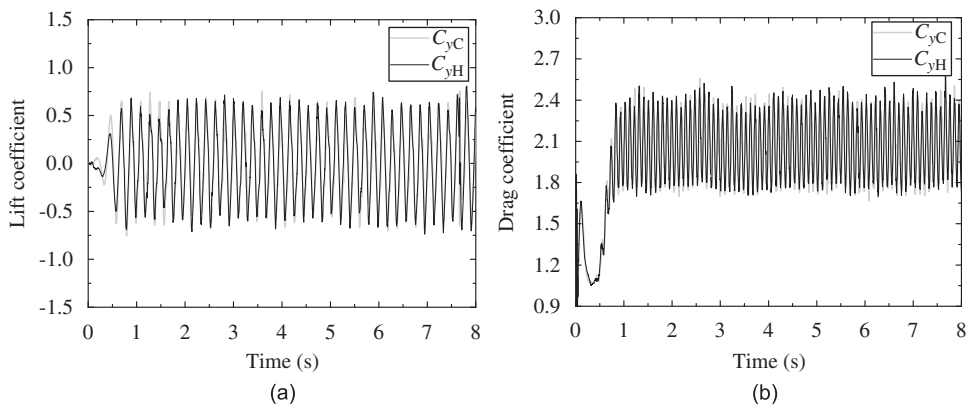


Fig. 5. Comparison of the aerodynamic coefficients obtained from the two simulation methods for a frequency ratio of 1.15: (a) lift coefficient and (b) drag coefficient.
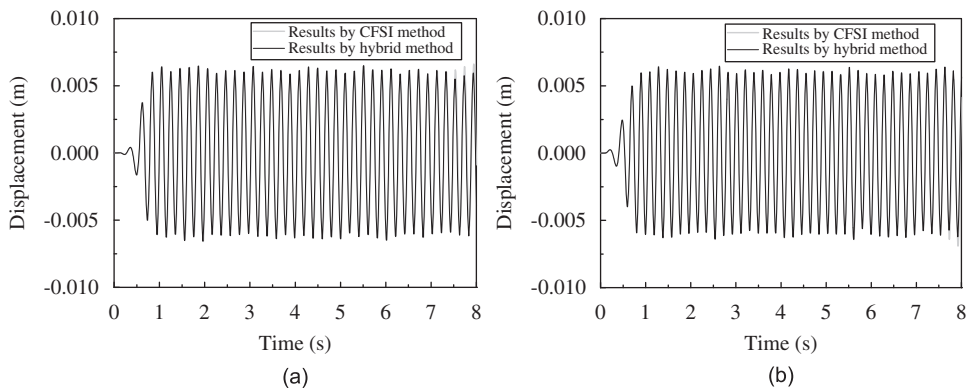


Fig. 6. Comparison of the oscillation displacement obtained from the two simulation methods: (a) 1.04 and (b) 1.15.

The Newmark–β method was used to solve Eq. (1), and the time histories of the cylinder displacement were obtained and compared to those that were calculated by the CFSI method as shown in Figs. 6(a) and (b) for frequency ratios of 1.04 and 1.15. The results of the hybrid approach are in good agreement with those of the CFSI method.
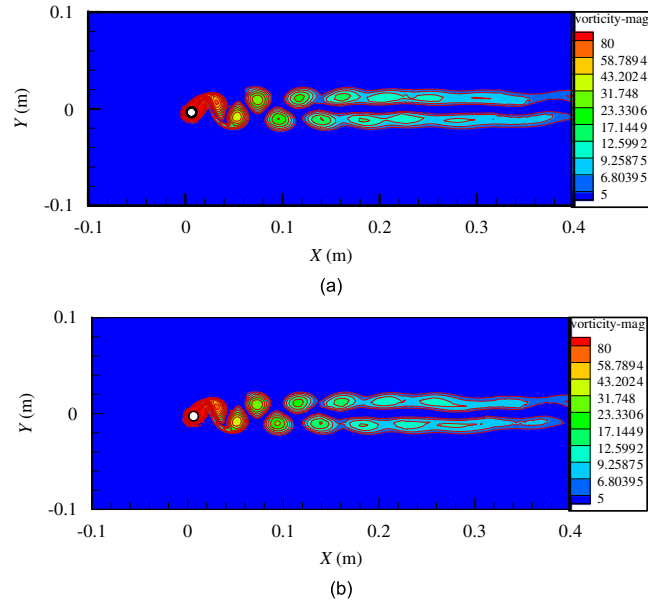
Fig. 7. Comparison of the vorticity contours obtained from the two simulation methods for a frequency ratio of 1.15: (a) CFSI approach and (b) hybrid approach.

Finally, the wake patterns were also compared using a frequency ratio of 1.15. Fig. 7 presents the vorticity contours that were obtained from these two methods at a time of 2.5 s. The two subgraphs show that both of the vortex shedding patterns exhibit the "2S" pattern (with slight differences).

The above comparison indicates that the cylinder response, the aerodynamic forces and the wake patterns that were obtained by using the two approaches are similar to one other. Therefore, the feasibility, reliability and accuracy of the proposed hybrid approach have been validated by this numerical example.

In addition, it took 8 h to calculate VIV of the cylinder by using CFSI approach (a PC with one Quad-Core CPU), while 7 h for the same investigation by using the hybrid approach. The computational efficiency of the hybrid approach is also verified through this simple example.

## 3. Hybrid approach for investigation on RWIV of a cable

### 3.1. Description of the RWIV measurement results in the wind tunnel tests

The RWIV of a stay cable was reproduced in the wind tunnel tests, and the rivulet oscillations around the circumference at one axial location on the cable were measured by using an ultrasonic transmission thickness measurement system (UTTMS) (Li et al., 2010), as shown in Fig. 8. The time-dependent spatial distribution of the water rivulets around the cable surface, i.e., the geometry and oscillation of water rivulets around the stay cable, was obtained using the UTTMS. The oscillation of the cable was measured using accelerometers. However, for the wind tunnel test of the RWIV of the stay cable under an artificial rainfall condition, the aerodynamic forces were difficult to measure using a pressure meter because the surface of the cable would have been affected by the presence of any sensors. For this study, the proposed hybrid approach was employed to obtain the aerodynamic forces acting on the oscillating cable, based on the previously measured cable motion in the wind tunnel tests.

The stay cable used in this study had the same geometry parameters as the cable in the wind tunnel test, i.e., the length and diameter of the cable were 2.0 and 0.1 m, respectively. The yaw and inclined angles were $\alpha = 22.5°$ and $\beta = 30°$, respectively, as shown in Fig. 9.

As the cable vibrated, the wind direction $\alpha_0$ varied in the experiment. The positive $x$ direction was used as the wind direction to define the aerodynamic coefficients. The lift coefficient $C_y$ and drag coefficient $C_x$ can be written as

$$C_y = \frac{F_y}{(1/2)\rho(U\cos\beta)^2 D}, \quad C_x = \frac{F_x}{(1/2)\rho(U\cos\beta)^2 D}, \tag{2}$$
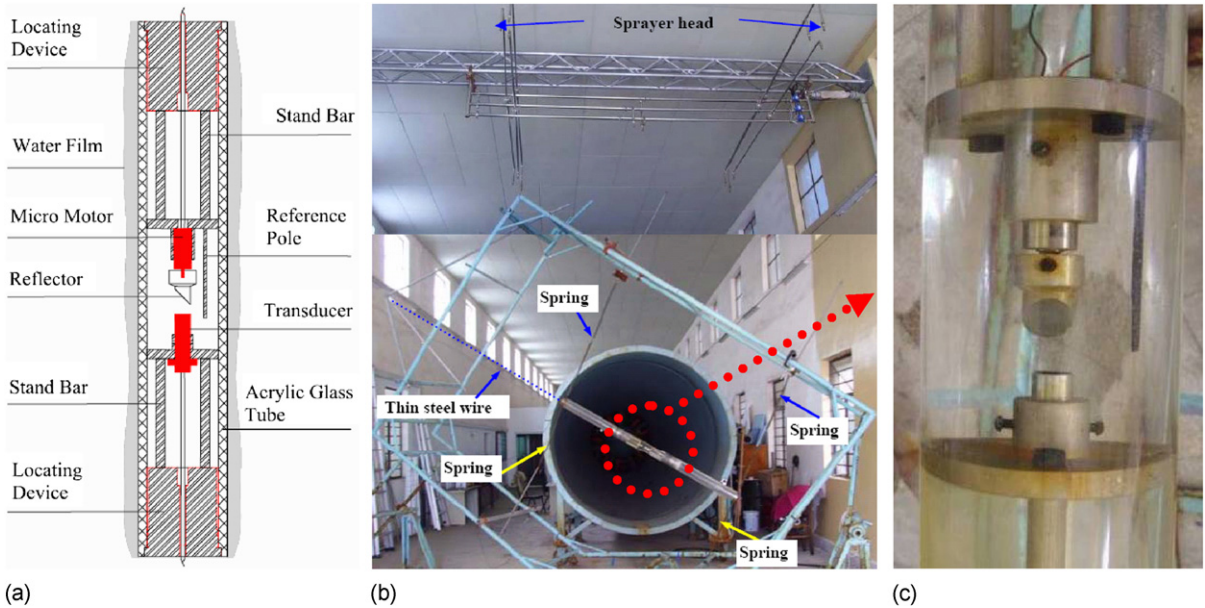
Fig. 8. Assembly of the wind tunnel test device and the UTTMS: (a) schematic diagram of UTTMS, (b) photograph of wind tunnel test device and (c) photograph of UTTMS.
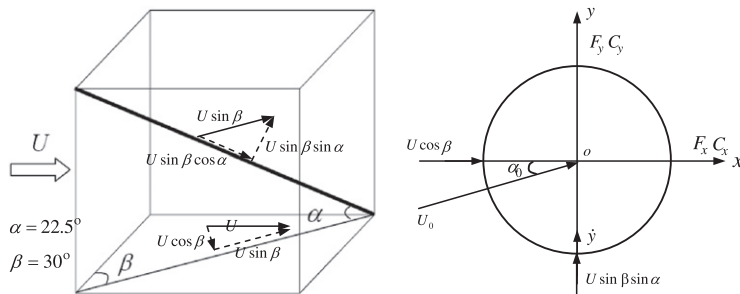


Fig. 9. Schematic diagram of the inclination angle and wind yaw angle of the cable model.

where $F_x$ and $F_y$ are the aerodynamic forces on the cable in the $x$ and $y$ directions, respectively; the other symbols are the same as previously defined. The mean inlet velocity was the same as the velocity used in the wind tunnel test, and a turbulent intensity of 5% was used for the inlet velocity.

The definition of the rivulet position and the schematic of the rivulet measurements from the UTTMS are shown in Fig. 10. The vibration amplitude of the stay cable versus the wind speed curve is shown in Fig. 11 and is compared with experimental results (Hikami and Shiraishi, 1988; Cosentino et al., 2003). The relation between vibration amplitude versus the wind speed used in this paper is similar to other researchers' results, with some differences in the amplitude and the wind speed range where the RWIV occurs. This difference can be attributed to the different parameters of the cable model and the test surroundings, such as the damping ratio, model weight, frequency, inclination angle, wind yaw angle, wind speed, turbulence intensity and rainfall intensity. Fig. 11 shows that when the wind speed is over 8.04 m/s or below 6.76 m/s, the RWIV of the stay cable does not occur; only when the wind speed is in the range of 6.76–8.04 m/s (such as 7.40 and 7.72 m/s) does RWIV occur. Meanwhile, the water rivulets display three different states for the three wind speed ranges, as shown in Figs. 12–14.

Fig. 12(a) shows the water rivulet distribution on the surface of the stay cable measured by UTTMS at the mid-span location of the stay cable along the axial direction for a wind speed of 6.76 m/s. Fig. 12(a) shows that the continuous upper rivulets did not flow along the axial direction of the cable and slide to the windward side, and the asymmetric slip of the upper rivulet may have been caused by the influence of an axial flow; the influence of the axial flow on the rivulet
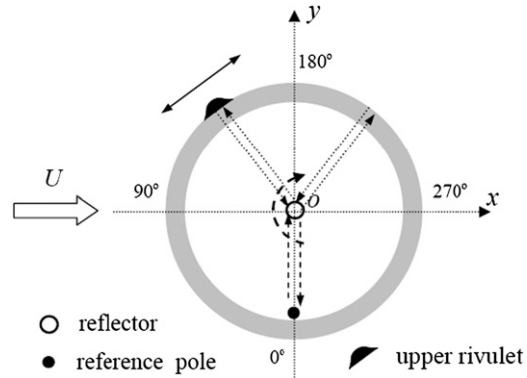
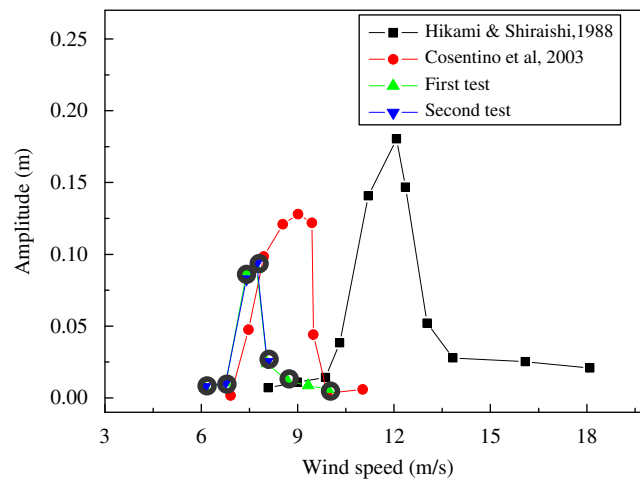Fig. 10. Schematic of the rivulet measurements by the UTTMS.



Fig. 11. Vibration amplitude versus wind speed (Li et al., 2010).

will be measured in a future test. This phenomenon is also shown in a snapshot of the water rivulet distribution at the same wind speed of 6.76 m/s in Fig. 12(b).

When the wind speed increases and exceeds the critical wind speed of 6.76 m/s, a continuous upper rivulet forms and oscillates along the circumferential direction of the cable model at a wind speed of 7.72 m/s, as shown in Fig. 13(a). At this wind speed, the RWIV of the cable model occurs, and the upper rivulet forms and results in a steady circumferential oscillation. A continuous lower rivulet also forms, but it is almost stationary in the circumferential direction. If the rain falls onto the surface of the cable model, then most of the raindrops immediately join the water rivulet, but a few raindrops may stop on the cable for some time, and the scattered points may be the thicknesses of these raindrops that are captured by the UTTMS. Fig. 13(b) also shows that there is an upper rivulet forming on the surface of the cable model.

As the wind speed continuously increases and exceeds the velocity range in which the RIVW of the cable model occurs, the upper rivulet still remains, but the steady circumferential oscillation of this rivulet gradually disappears (as shown in Fig. 14) at a wind speed of 8.04 m/s. Compared with Fig. 13(a), the lower rivulet is also stationary, but the oscillation of the upper rivulet is quite different, i.e., in one case it is disordered and unsystematic (Fig. 14(a)), and in the other it is regular and similar to a simple harmonic vibration (Fig. 13(a)).

### 3.2. Models

The lower rivulet was neglected in the present model for the numerical simulation of the hybrid approach according to the analysis of the rivulet that was stated above. The statistical mean shape of the upper rivulet is approximately an isosceles trapezoid with a hemline of 8 mm, a height of 0.509 mm and a bottom angle of 45° (Li et al., 2010). The wind speed range can be classified into three conditions: 6.12 and 6.76 m/s are defined as condition 1 with no continuous
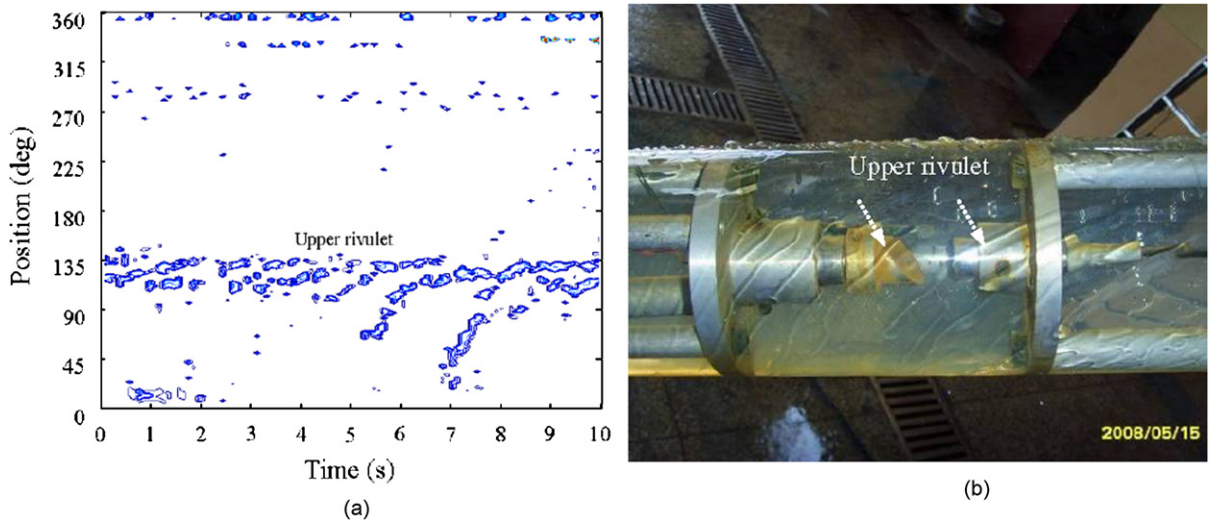
Fig. 12. Water rivulet distribution at a wind speed of 6.76 m/s: (a) water rivulet contour along the circumferential direction measured by the UTTMS and (b) a snapshot of the water rivulet distribution.
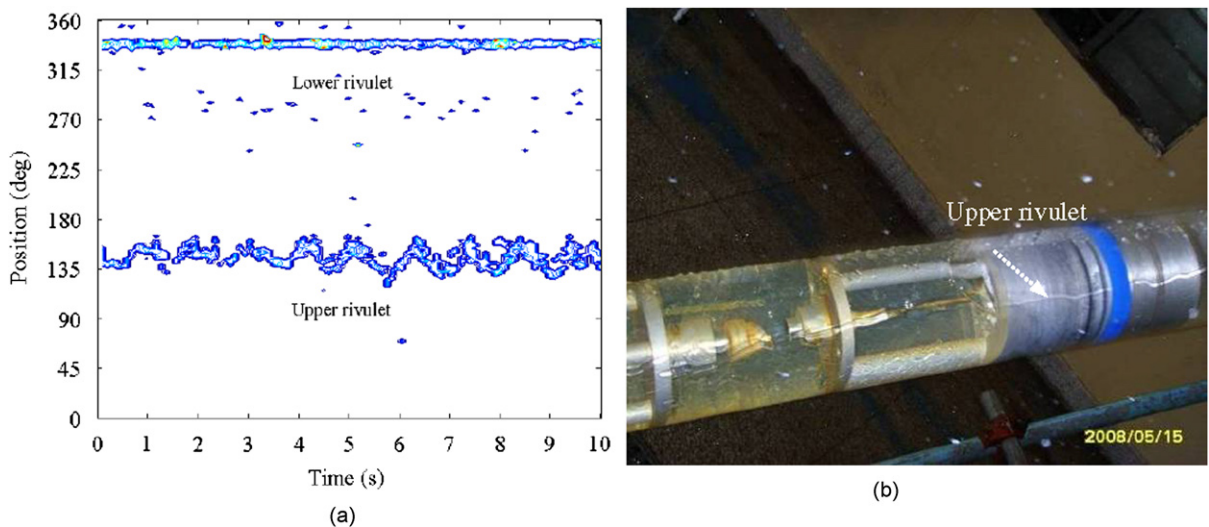


Fig. 13. Water rivulet distribution at a wind speed of 7.72 m/s: (a) water rivulet contour along the circumferential direction measured by the UTTMS and (b) a snapshot of the water rivulet distribution.

upper rivulet; 7.40 and 7.72 m/s are defined as condition 2 with a regular continuous upper rivulet; and 8.04, 8.69 and 9.94 m/s are defined as condition 3 with a disordered and unsystematic upper rivulet.

Fig. 15 shows the computational domain of the CFD numerical simulation for the RWIV of the cable model using the hybrid approach. The cuboid-shaped computational region is 3.0 m long, 3.0 m wide and 1.6 m high. The distances from the centre of the model axis to the inlet and the outlet are 1.0 and 2.0 m, respectively; the distance from the centre of the model axis to the upper boundary (or lower boundary) of the computation domain is 1.0 m; and the distance from the model axis to the left boundary (or right boundary) of the computation domain is 1.5 m. The boundary conditions are defined as follows: the inlet is set as "velocity inlet"; the outlet is set as "outflow" and is a fully developed outlet boundary; the upper, lower, left and right boundaries are set as "symmetry"; and the surfaces of the cable model and the upper rivulet are set as "wall". The fluid velocity of the surfaces of the cable model and the upper rivulet are equal to the measured velocities of the cable model and the upper rivulet, which were assigned by the UDFs. The SST $k-\omega$ turbulence model based on the RANS method was used to simulate the behaviour of turbulent flow in the CFD
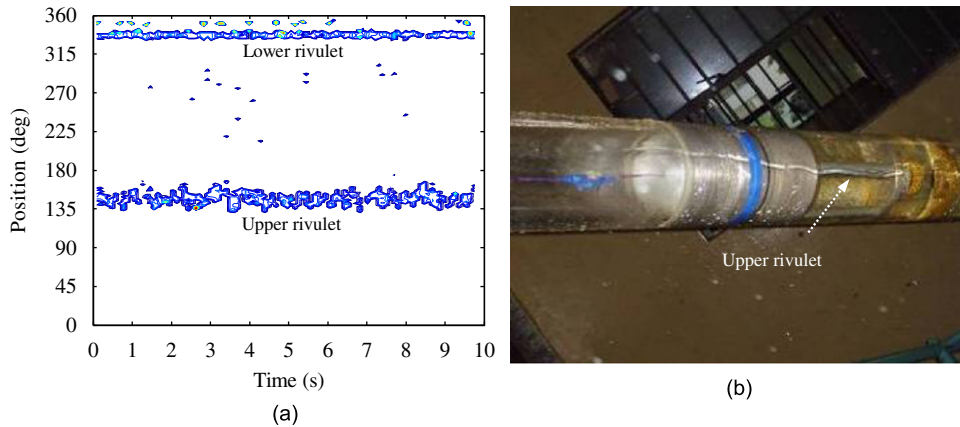
Fig. 14. Water rivulet distribution at a wind speed of 8.04 m/s: (a) water rivulet contour along the circumferential direction measured by the UTTMS and (b) a snapshot of the water rivulet distribution.
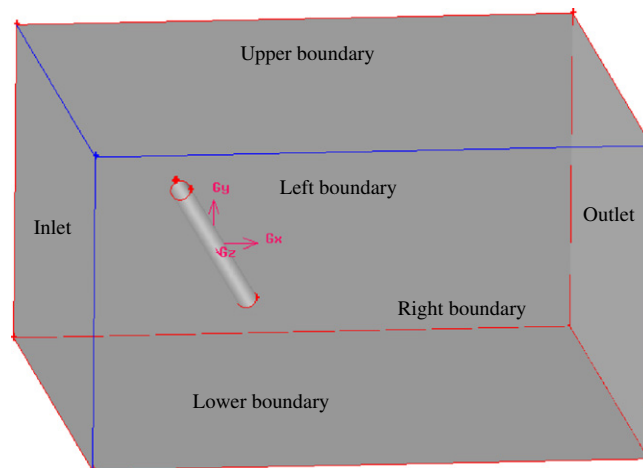


Fig. 15. Computation domain of the RWIV of the cable model for the hybrid approach.

numerical simulation. The convergence criteria of the absolute residual were set as $10^{-4}$ for the three velocity components and $10^{-5}$ for the $k$ and $\omega$ equations, because the convergent steps for three velocity components were much larger than the other parameters. For this investigation, the number of grid cells was nearly 1 200 000 and the computational time (for 50 s time history) for each wind speed case was about 170 h using two Quad-Core CPUs. In the computational process, the residuals of each variable were steadily maintained below the set value.

For conditions 2 and 3, there was some relative motion between the upper rivulet and the stay cable, and thus the system was classified into the following: the flow field, the stay cable and the upper rivulet substructures, and the cable and rivulet models are shown in Fig. 16. The upper rivulet was assumed to be straight along the axial direction of the cable model, i.e., the vibration of the upper rivulet along the axis direction of the cable model is in-phase.

The rivulets did not flow along the axial direction of the cable and slide to the windward side for condition 1, as shown in Fig. 12, and thus the system was only classified as a fluid substructure and a stay cable substructure with many small sliding rivulets. The cable and rivulets models are shown in Fig. 17. The sliding rivulets are fixed on the surface of the stay cable (i.e., vibrate along with the cable model) and have no relative motion with respect to the stay cable.

### 3.3. Moving boundary of the flow field

There are seven cases according to the wind speed as follows: 6.12, 6.76, 7.40, 7.72, 8.04, 8.69 and 9.94 m/s. Figs. 18 and 19 show the measured oscillations and the frequency responses of the cable model and the upper rivulet at a wind
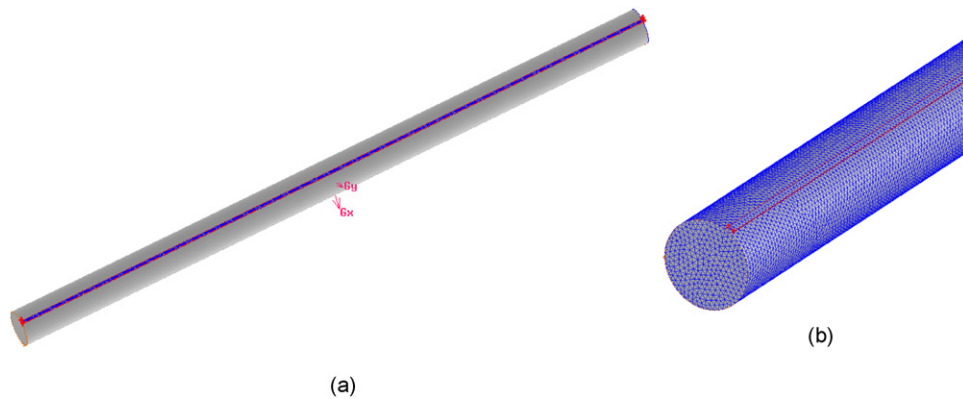
Fig. 16. Model of the cable and grid partition for conditions 2 and 3: (a) cable and rivulet models and (b) local grid partition.
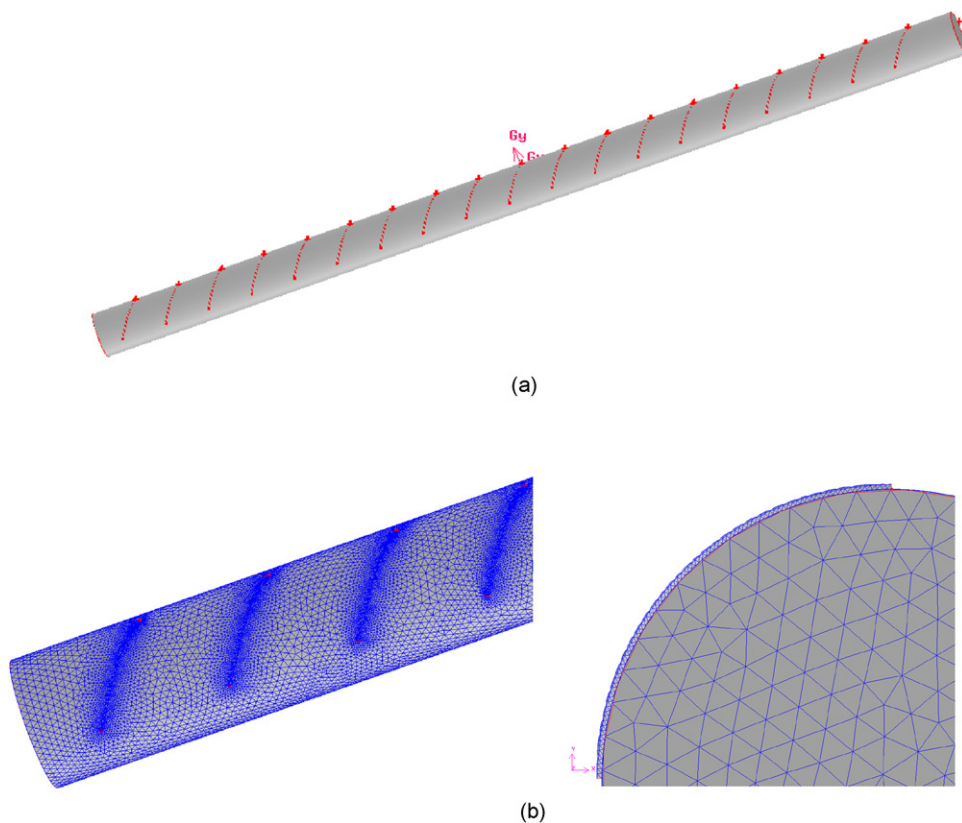


Fig. 17. Model of cable and grid partition for condition 1: (a) cable and rivulet models and (b) local grid partition.

speed of 7.72 m/s in the wind tunnel test. The results indicate that both the frequencies of cable vibration and rivulet oscillation are identical to the natural frequency of the stay cable when the RWIV occurs at a wind speed of 7.72 m/s. The measured oscillations of the cable and rivulet shown in Figs. 18(a) and 19(a) were added to the flow field as moving boundaries, which are interfaces between the flow fields of the stay cable and the upper rivulet, respectively. A wind speed of 7.40 m/s is close to 7.72 m/s, and thus the moving boundaries of 7.40 m/s are not shown here.

Figs. 20 and 21 show the displacement responses of the cable and rivulet in the time domain and frequency domain at a wind speed of 8.69 m/s. The results indicate that the frequency of the cable vibration is simply the natural frequency of
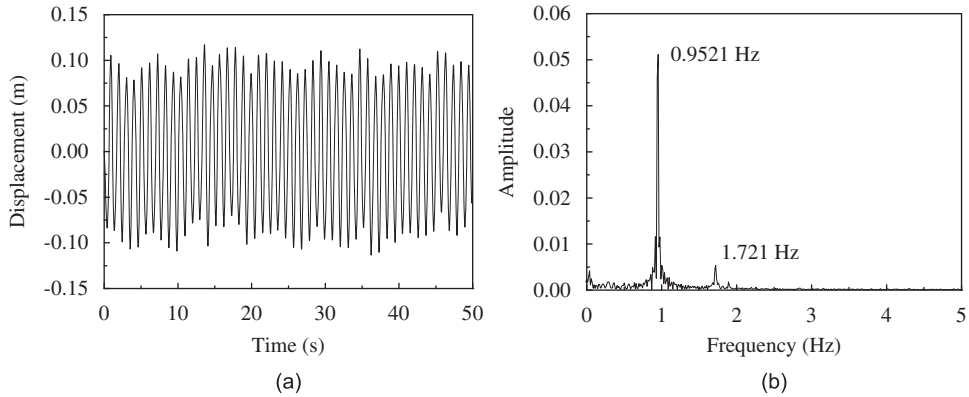
Fig. 18. Transverse displacement response of the cable model at a wind speed of 7.72 m/s: (a) time histories and (b) frequency spectrum analysis.
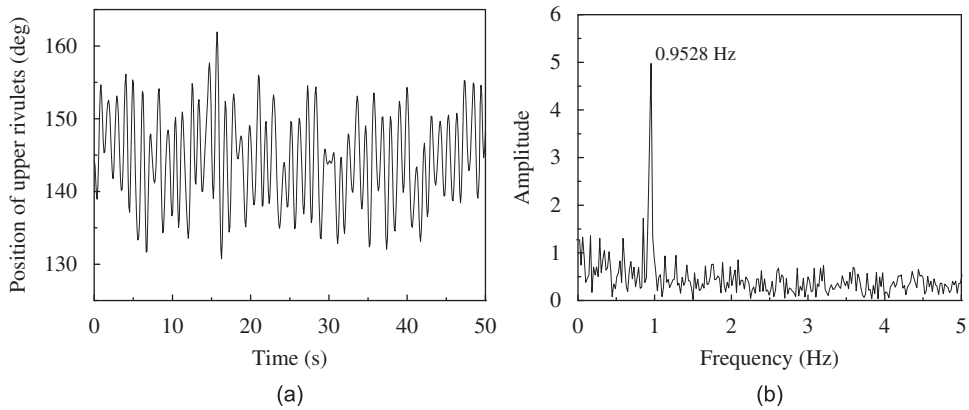


Fig. 19. Upper rivulet oscillation response along the circumferential direction at a wind speed of 7.72 m/s: (a) time histories and (b) frequency spectrum analysis.
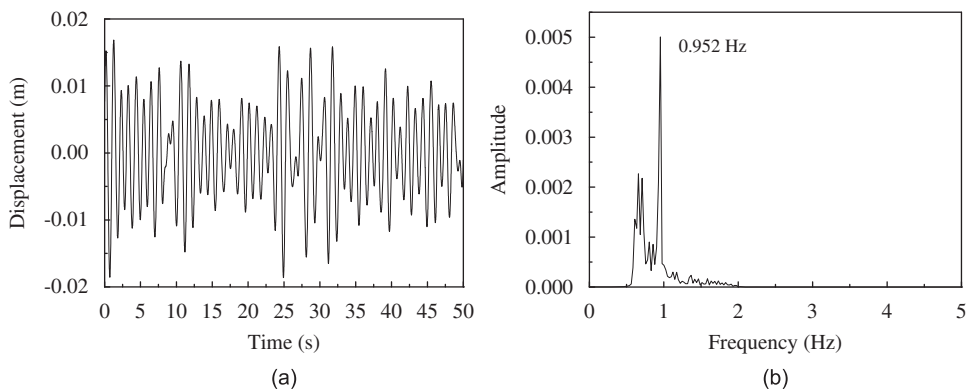


Fig. 20. Transverse displacement response of the cable model at a wind speed of 8.69 m/s: (a) time histories and (b) frequency spectrum analysis.

the stay cable with a small vibrational amplitude, but there is no dominant frequency for the rivulet oscillation when the wind speed is 8.69 m/s. The cable vibration and the rivulet oscillation at 8.04 and 9.94 m/s have similar characteristics to those at 8.69 m/s. Also, the vibrations of the cable and the rivulet shown in Figs. 20(a) and 21(a) were added to the flow field as the moving boundaries.
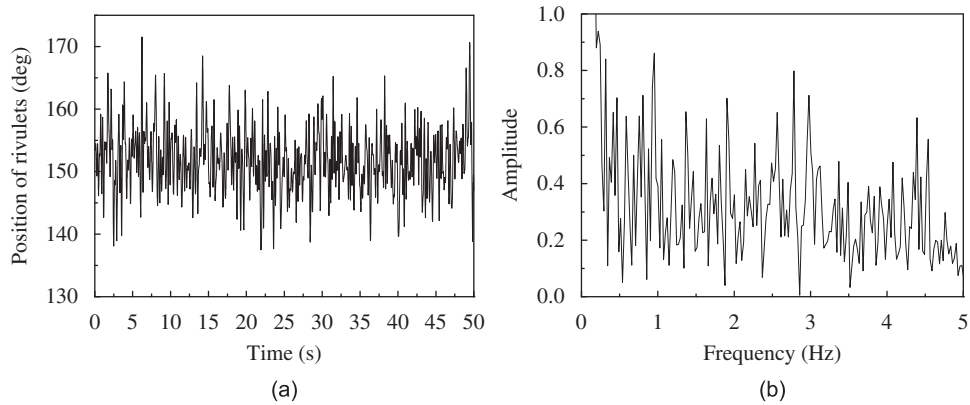
Fig. 21. Upper rivulet oscillation response along the circumferential direction at a wind speed of 8.69 m/s: (a) time histories and (b) frequency spectrum analysis.
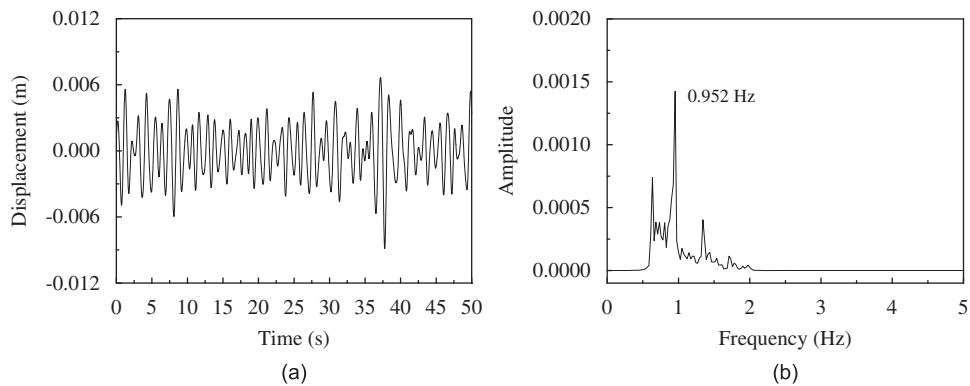


Fig. 22. Transverse displacement response of the cable model at a wind speed of 6.12 m/s: (a) time histories and (b) frequency spectrum analysis.

Fig. 22 shows the RWIV of the stay cable at a wind speed of 6.12 m/s. The cable vibration amplitude is very small, but there is a dominant frequency of 0.952 Hz. The cable and rivulet have the same boundary motion as shown in Fig. 22(a), while the surface of the cable (with a number of fixed rivulets) and grids of the flow field are different from those for conditions 2 and 3. The same model can be used for the case of a wind speed of 6.76 m/s.

## 4. Results and analysis

### 4.1. Aerodynamic coefficients

The aerodynamic behaviour of the flow field with a moving boundary was calculated using Fluent 6.3, and the aerodynamic forces of the cable were obtained by integrating the pressure on the cable surface; the aerodynamic coefficients can be further calculated by using Eq. (2). Fig. 23 shows the time histories and frequency spectra of the lift coefficients at various wind speeds (the respective means for the seven cases have been subtracted). The initial large variant in the lift coefficient histories may be caused by the absence of steady-state conditions in the numerical simulation.

A statistical analysis for the lift coefficients was performed, and the root mean square (rms) of each lift coefficient history was obtained, as shown in Fig. 24. Figs. 23 and 24 show that when the RWIV of the cable occurred at wind speeds of 7.40 and 7.72 m/s, the lift coefficient had the largest rms and amplitude in time history with a dominant frequency of 0.952 Hz, which is the natural frequency of the cable. When the wind speeds were 6.12 and 6.76 m/s (at which RWIV of the cable does not occur), the lift coefficient had a dominant frequency of 0.952 Hz and a lower
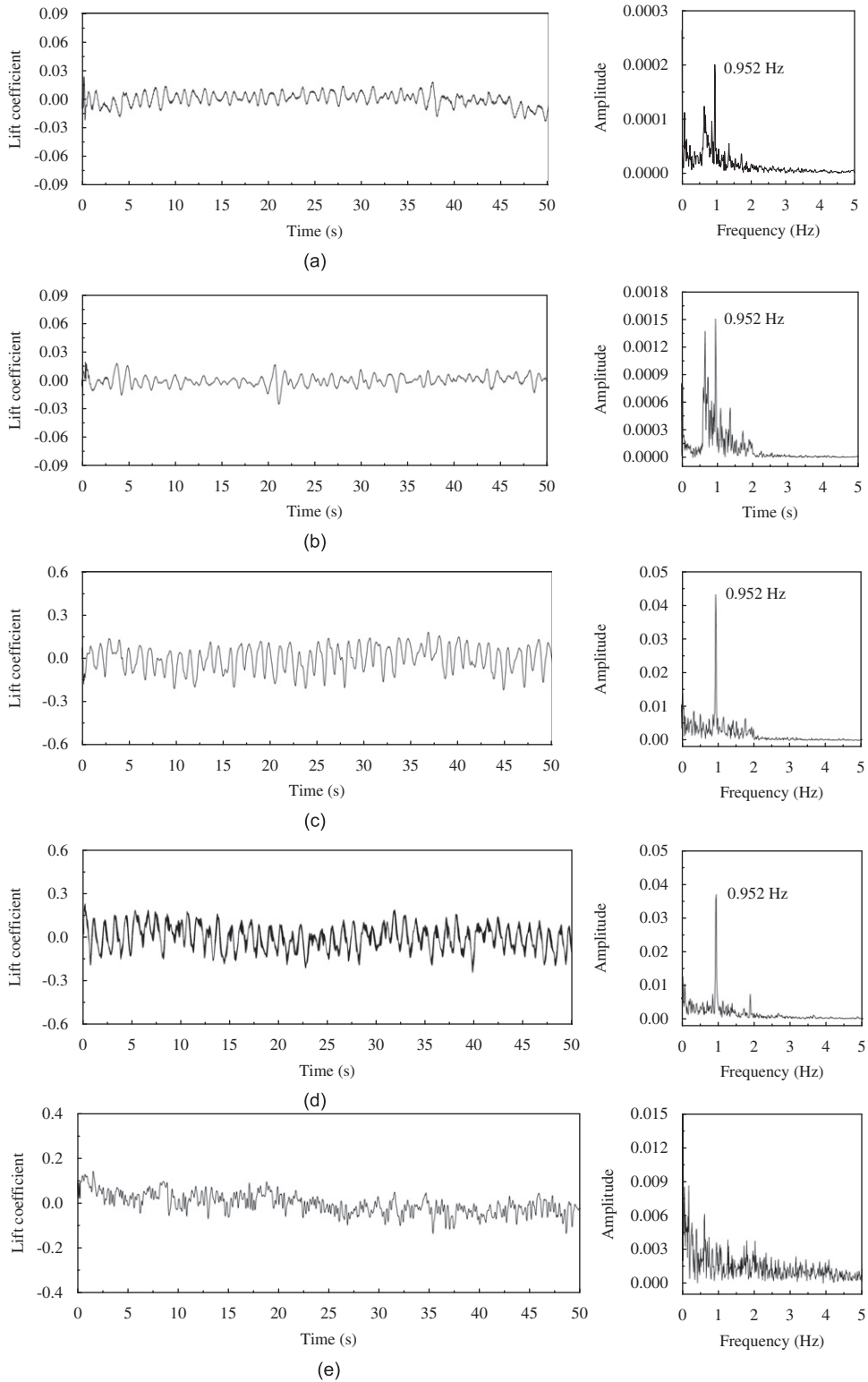
Fig. 23. Time histories and frequency spectra of the lift coefficients of the stay cable at various wind speeds: (a) 6.12 m/s, (b) 6.76 m/s, (c) 7.40 m/s, (d) 7.72 m/s, (e) 8.04 m/s, (f) 8.69 m/s and (g) 9.94 m/s.
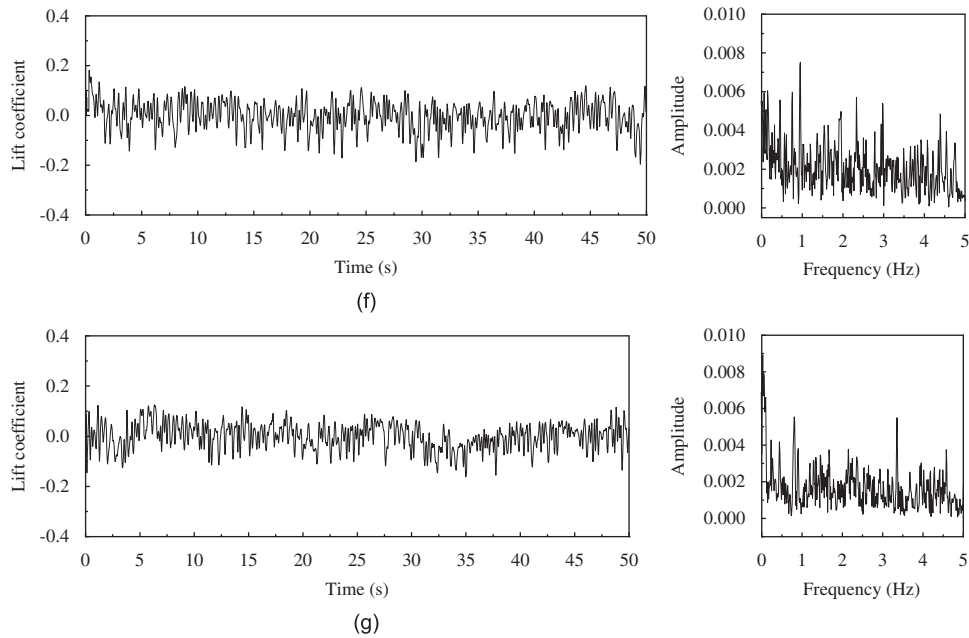
Fig. 23. (*Continued*)

frequency (which may be system noise). The rms and amplitude in the time history of the lift coefficient are the smallest ones. When the wind speeds were 8.04, 8.69 and 9.94 m/s (at which the RWIV of the cable does not occur), the lift coefficient does not have a dominant frequency but has a larger rms value.

The difference between the lift coefficient responses may be caused by different rivulet oscillations, and the conditions for three wind speed regions are as follows: the regular rivulet oscillation with a larger amplitude will induce a larger regular variation in the wind pressure on the surface of the cable at 7.40 and 7.72 m/s; the irregular rivulet oscillation with a relatively larger amplitude will induce a larger but irregular variation in the wind pressure on the surface of the cable at 8.04, 8.69 and 9.94 m/s; and no continuous upper rivulet on the cable surface will induce a very small change in the lift coefficient amplitude at wind speeds of 6.12 and 6.76 m/s.

### 4.2. Cable vibration response

For further verification of the calculation, the lift force was applied to the SDOF model of the stay cable in the cross-flow direction (obtained according to the lift coefficient time history as shown in Fig. 23 and Eq. (2)). The vibration response of the cable under various test wind speeds was obtained using Eq. (1) and is shown in Fig. 25. For comparison, the experimental results are also shown in Fig. 25.

The comparison indicates that the results calculated by Eq. (1) are very close to the experimental results at wind speeds of 7.40 and 7.72 m/s. However, some differences between the numerical results and the experimental results at other wind speeds are observed, particularly for a wind speed of 8.69 m/s. The calculation results are more stable than the experimental results. The above phenomenon can be attributed to the fact that the upper rivulets around the circumferential direction were not oscillating synchronically or sliding and might have behaved randomly. Asynchronous oscillation or sliding of the rivulet induces irregular aerodynamic forces and vibration responses of the cable.

### 4.3. Aerodynamic damping

The aerodynamic force adds an equivalent aerodynamic damping ratio to the stay cable. The occurrence of the RWIV may be a result of the aerodynamic damping, which may result in the total damping of the stay cable to a negative value. The most common method for defining the equivalent damping ratio is to allow the energy dissipated in a vibration cycle of the actual structure to be identical to that of an equivalent damping system. The equivalent
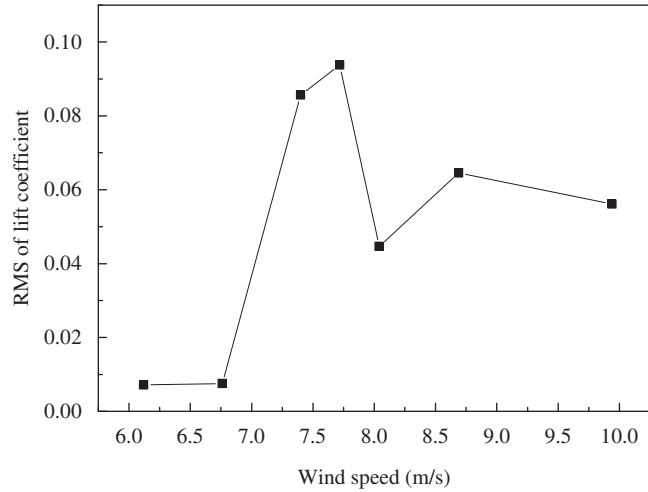
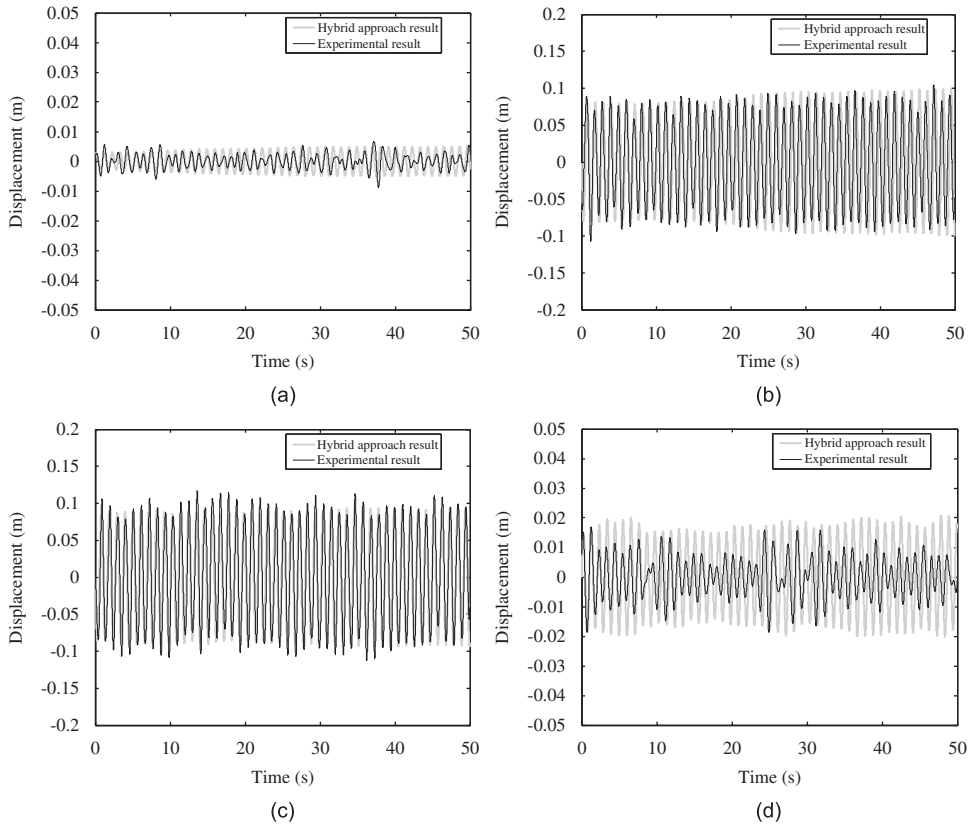Fig. 24. Rms of lift coefficient versus wind speed.



Fig. 25. Comparison of cable vibration responses obtained by numerical and experimental investigations: (a) 6.12 m/s, (b) 6.76 m/s, (c) 7.40 m/s, (d) 7.72 m/s, (e) 8.04 m/s, (f) 8.69 m/s and (g) 9.94 m/s.

damping ratio can be expressed by the following equation (Chopra, 2000):
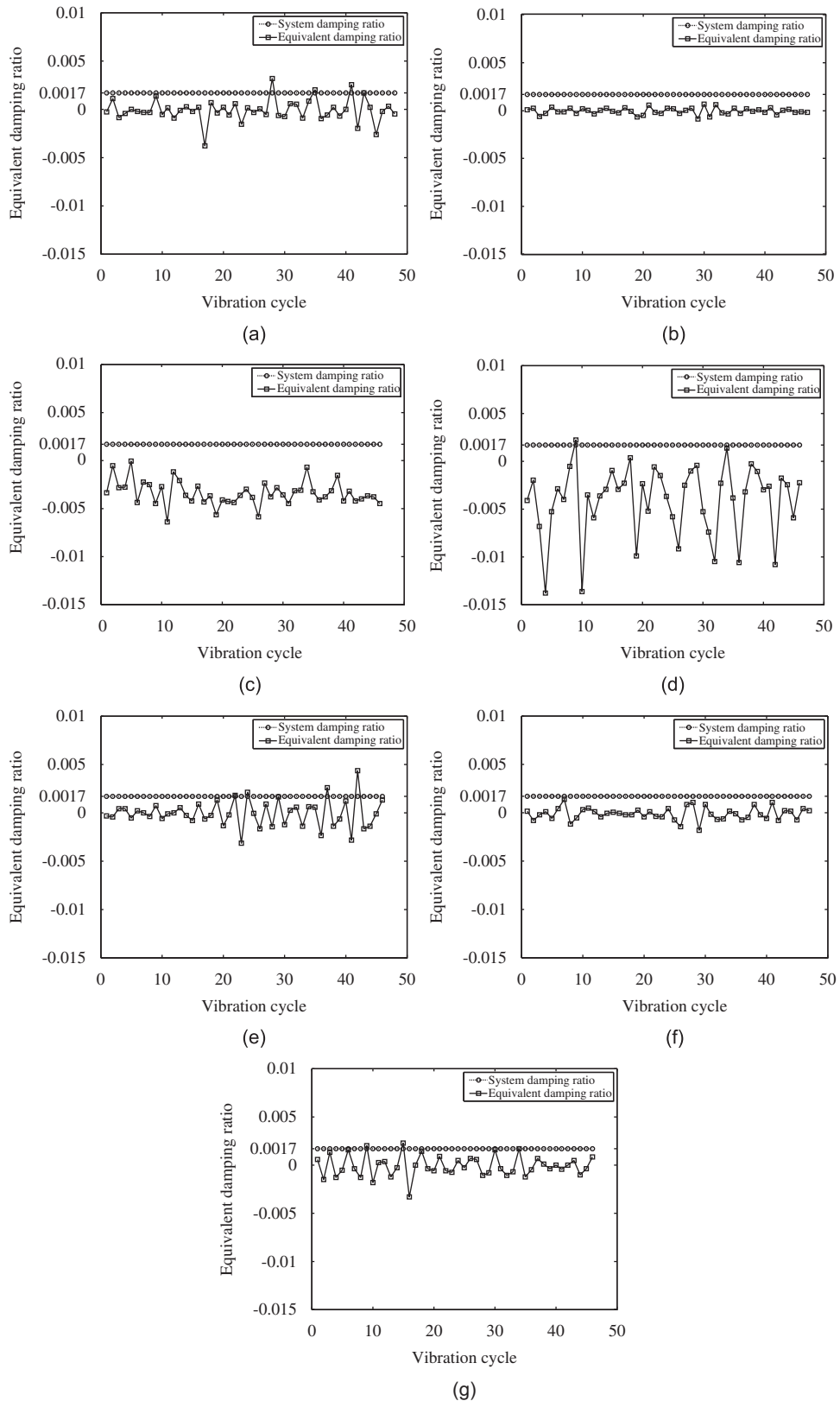
$$\xi_{eq} = \frac{E_D}{4\pi E_s},$$

(3)

Fig. 26. Comparison of the equivalent damping ratio applied by aerodynamic forces and system damping ratio at different speeds: (a) 6.12 m/s, (b) 6.76 m/s, (c) 7.40 m/s, (d) 7.72 m/s, (e) 8.04 m/s, (f) 8.69 m/s and (g) 9.94 m/s.

where $E_D$ is the energy dissipated by the aerodynamic force in one cycle, $E_s = Ku_0^2/2$ is the elastic strain energy for one cycle of the cable and $u_0$ is the amplitude of the cable transverse oscillation $y$ in Eq. (1).

The system damping ratio of the stay cable under a free vibration with zero wind speed is 0.0017. The equivalent damping ratio added by the aerodynamic forces and system damping ratio at different speeds are shown in Fig. 26. The horizontal axis contains the vibration cycle; the vertical axis contains the equivalent damping ratio and system damping ratio for each period of the cable oscillation. The equivalent damping ratio by the aerodynamic force is negative, and the absolute values are larger than the system damping ratio of 0.0017 in most of the oscillating periods at wind speeds of 7.40 and 7.72 m/s in which the RWIV of the stay cable occurs. For other wind speeds, the equivalent damping ratio by the aerodynamic force was smaller than the system damping ratio in most of the oscillating periods. The occurrence of the RWIV indicates a close relationship between the equivalent damping ratio and the aerodynamic force.

The mean equivalent damping ratio for all of the cycles was obtained from a statistical analysis for each of the wind speeds. Fig. 27 indicates that the mean equivalent damping ratio varies with the wind speed. When the wind speeds are 7.40 and 7.72 m/s, the mean equivalent damping ratios are −0.0034 and −0.0038, respectively, and the absolute values are larger than the system damping ratio of 0.0017. At other wind speeds, the absolute values of the mean equivalent damping ratios are less than the system damping ratio, and thus the total damping ration is positive. The RWIV of the cable may have been induced by the large negative equivalent damping that was generated by the aerodynamic force.

## 4.4. Aerodynamic coefficient model

To model the aerodynamic coefficient, the lift coefficient histories of seven cases are connected as shown in Fig. 28. This is not a true time history from 0 to 350 s. Instead, each time history was for a duration of 50 s; thus, the total time for the seven cases is 350 s.

The lift coefficient $C_y(y, \dot{y}, \varphi, \dot{\varphi}, t)$ in Eq. (1) is a nonlinear function of the cable vibration and rivulet oscillation and can be expressed as a polynomial. The second degree and higher degrees can be omitted with respect to the symmetric
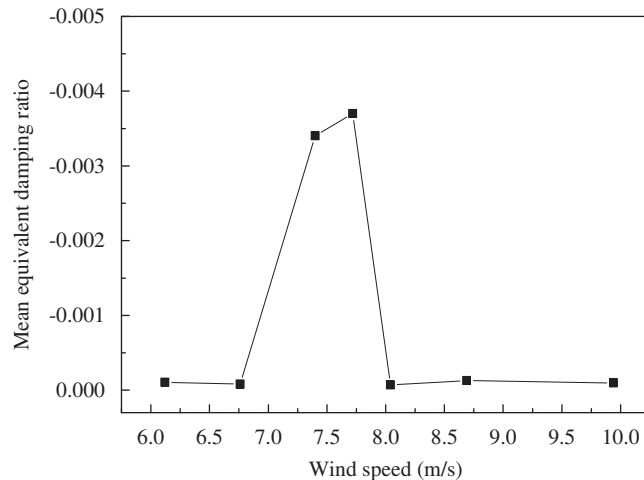


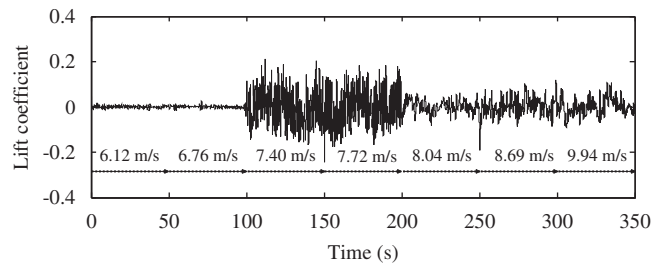Fig. 27. Equivalent damping ratio by the aerodynamic force at different speeds.



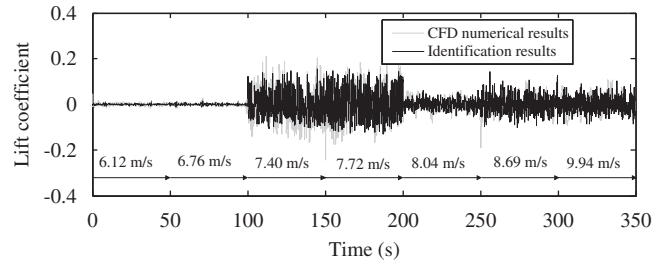Fig. 28. Lift coefficient histories of seven cases.

Fig. 29. Lift coefficient histories comparison of seven cases between CFD and identification.

characteristic of the lift coefficient history (Naprstek et al., 2007). The nonlinear lift coefficient model $C_y(y, \dot{y}, \varphi, \dot{\varphi}, t)$ of the stay cable under the RWIV can be expressed as follows:

$$C_y = c_1\dot{y} + c_2 y + c_3\varphi\dot{y} + c_4\dot{y}^3 + c_5 y^3 + c_6\varphi + c_7\dot{\varphi}, \tag{4}$$

where $y$ and $\dot{y}$ are the displacement and velocity of the cable vibration, respectively, $\varphi$ and $\dot{\varphi}$ are the angle and angular velocity of the rivulet oscillation, respectively, and $c_1$, $c_2$, $c_3$, $c_4$, $c_5$, $c_6$ and $c_7$ are coefficients. The coefficients of the nonlinear lift coefficient model $C_y(y, \dot{y}, \varphi, \dot{\varphi}, t)$ were identified through a nonlinear least-squares method derived from the entire time histories of the response (350 s for seven cases), as illustrated in Fig. 28, and can be expressed as follows:

$$C_y = 0.169\dot{y} + 0.0823y + 0.755\varphi\dot{y} - 0.246\dot{y}^3 + 13.933y^3 + 0.294\varphi + 0.00253\dot{\varphi}. \tag{5}$$

A comparison of the aerodynamic coefficient obtained by using the hybrid approach and parameter identification (Eq. (5)) is shown in Fig. 29. The identification results at wind speeds of 6.12, 6.76, 7.40 and 7.72 m/s are better than the other cases.

The $c_2$ parameter is related to the vibration frequency of the stay cable and is equal to 0.0823. It is small (relative to the velocity term $c_1$ parameter) and indicates that the change in the stiffness of the cable that was caused by the aerodynamic force is small. Therefore, the vibration frequency of the cable does not shift much when the RWIV occurs. Furthermore, the change in mass by the raindrops and water rivulets on the cable surface can also be neglected.

## 5. Discussion

Wind and rain simultaneously existed in the wind tunnel tests, but only the wind field was simulated and the rain field was neglected in the hybrid approach. Therefore, the influence of rain on the wind was not considered. The air density for a rainy condition may change by about 0.05%, which can be neglected by analysing the features of raindrops in a typhoon as observed in the Guangzhou area of China in 1995. However, rain not only plays a key role in the formation of the rivulet (which results in a change in the aerodynamics), it also may have an impact on the wind field, particularly on the wind direction, wind speed and wind turbulence. The inlet velocity used in the CFD numerical simulation of the hybrid approach does not completely reproduce the velocity in the wind tunnel test (at the contraction section of the TJ-1 boundary layer wind tunnel in Tongji University, China). The distribution of the mean wind speeds at the exit of wind tunnel is not uniform. For example, the wind speed at the central point of the exit section is 6.64 m/s, while the maximum and minimum wind speeds at the measurement points at the same section are 8.08 and 4.70 m/s, respectively. For simplicity, a uniform inlet wind speed distribution was employed in the CFD numerical simulation of the hybrid approach. Additionally, it is difficult to determine if the turbulent intensity is capable of an actual wind field in the wind tunnel test at the present stage. Further analysis will be performed to obtain the rain-wind coupled field model through wind tunnel tests or CFD techniques.

The behaviour of water on the surface of a stay cable in the wind tunnel test is very complicated. The entire process includes raindrops falling, impacting on the cable surface, rebounding from the cable surface, attaching to the cable surface, colliding and converging on the cable surface, and forming into water rivulets as well as random distribution or random oscillations on the surface of the stay cable. This is a complicated multiphase medium problem that includes gas (wind), liquid (rain) and solid (cable). However, because this is not the emphasis and goal in this paper, the numerical simulation starts from the formed rivulet or by directly determining the status of the raindrop on the surface of the stay cable. The oscillation or sliding states of the rivulet are assumed to be ideal in the calculation; however, they are

irregular and stochastic in the wind tunnel test. The upper rivulet is assumed to be a straight line for conditions 2 and 3, but it may change along the axial direction of the cable. The upper rivulets are set to slide downward along a 45° angle for condition 1 while they may also slide stochastically along the cable.

The noise is nearly the same for all of the conditions, and thus the ratio of the noise to the vibration signal measured by the accelerometers for conditions 1 and 3 is larger than that of condition 2 because the oscillation amplitude of the cable for condition 2 is larger. Therefore, the influence of noise on the moving boundary in the numerical simulation for condition 2 is smaller than that of the other two conditions.

All of the above-mentioned limitations can cause errors in the numerical simulation results. Regardless of these limitations, the hybrid approach is a potential tool to obtain the aerodynamic forces for the RWIV, and the accuracy of the numerical simulation for RWIV is acceptable. These limitations will be improved upon in future studies.

The following conditions for the occurrence of the RWIV of the cable should be satisfied according to the above analysis and the test results by using artificial rivulets as discussed in the relevant literature (Gu et al., 2009): (1) The upper rivulet must form on the cable surface. The appropriate wind speed and rainfall are required to allow the upper rivulet to form. (2) The position of the upper rivulet should be located within a certain range on the cable surface. If the above conditions are met, then an aerodynamic force with the natural frequency of the cable is generated by the interaction between the cable rivulet and air, which adds negative damping to the cable. The cable and rivulet oscillate in resonant movements, and thus the RWIV of the cable is excited by the negative aerodynamic damping force with resonant frequency.

## 6. Conclusions

This paper presents a hybrid approach of tests combined with CFD to obtain the aerodynamic force of a stay cable under RWIV. The following conclusions were obtained from this study:

1. The feasibility, reliability, accuracy and computational efficiency of the hybrid approach are validated through comparison with CFSI for investigation on VIV of a circular cylinder and with the wind tunnel test for investigation on RWIV of a stay cable.
2. Over the wind speed range of the RWIV, a more accurate aerodynamic force can be obtained, and it has a dominant frequency (i.e., natural frequency of the cable) and a large amplitude. Below this wind speed range, the aerodynamic force has a primary frequency but a small amplitude, and above this wind speed range, the aerodynamic force has a large amplitude but no dominant frequency.
3. If RWIV occurs, then the equivalent damping ratio added by the aerodynamic force is negative, and its absolute value is larger than the system damping ratio in most of the oscillation periods. For other wind speeds in which RWIV cannot occur, the equivalent damping ratio achieved by the aerodynamic force is also negative, but its absolute value is smaller than the system damping ratio for most of the oscillation periods.
4. The coefficients of the nonlinear aerodynamic force model were identified by using a nonlinear least-squares technique based on the aerodynamic coefficients and vibration of the cable obtained by using the hybrid approach, and it is in good agreement with the calculated results for most of the test cases.

## References

Bosdogianni, A., Olivari, D., 1996. Wind- and rain-induced oscillations of cables of stayed bridges. Journal of Wind Engineering and Industrial Aerodynamics 64, 171–185.
Chopra, A.K., 2000. In: Dynamics of Structures: Theory and Applications to Earthquake Engineering second ed Prentice-Hall, Englewood Cliffs, NJ, USA.

Cosentino, N., Flamand, O., Ceccoli, C., 2003. Rain-wind-induced vibration of inclined stay cables, Part I: experimental investigation and physical explanation. Wind and Structures 6 (6), 471–484.

Dong, S.J., Karniadakis, G.E., 2005. DNS of flow past a stationary and oscillating cylinder at Re = 10000. Journal of Fluids and Structures 20, 519–531.

Flamand, O., 1995. Rain-wind-induced vibration of cables. Journal of Wind Engineering and Industrial Aerodynamics 57, 353–362.

Griffin, O.M., Votaw, C.W., 1972. The vortex street in the wake of a vibrating cylinder. Journal of Fluid Mechanics 51 (1), 31–48.

Griffin, O.M., Ramberg, S., 1974. The vortex-street wakes of vibrating cylinders. Journal of Fluid Mechanics 66 (3), 553–576.

Gu, M., Du, X.Q., 2005. Experimental investigation of rain-wind-induced vibration of cables in cable-stayed bridges and its mitigation. Journal of Wind Engineering and Industrial Aerodynamics 93, 79–95.

Gu, M., Du, X.Q., Li, S.Y., 2009. Experimental and theoretical simulations on wind-rain-induced vibration of 3-D rigid stay cables. Journal of Sound and Vibration 320, 184–200.

Hikami, Y., Shiraishi, N., 1988. Rain-wind induced vibrations of cables in cable stayed bridges. Journal of Wind Engineering and Industrial Aerodynamics 29, 409–418.

Koopman, G.H., 1967. The vortex wakes of vibrating cylinders at low Reynolds numbers. Journal of Fluid Mechanics 28 (3), 501–512.

Li, F.C., Chen, W.L., Li, H., Zhang, R., 2010. An ultrasonic transmission thickness measurement system for study of water rivulets characteristics of stay cables suffering from wind-rain-induced vibration. Sensors and Actuators A: Physical 159 (1), 12–23.

Matsumoto, M., Shiraishi, N., Kitazawa, M., Knisely, C., Shirato, H., Kim, Y., Tsujii, M., 1990. Aerodynamic behavior of inclined circular cylinders-cable aerodynamics. Journal of Wind Engineering and Industrial Aerodynamics 33, 63–72.

Matsumoto, M., Shirashi, N., Shirato, H., 1992. Rain-wind-induced vibration of cables of cable-stayed bridges. Journal of Wind Engineering and Industrial Aerodynamics 41–42, 2011–2022.

Matsumoto, M., Saitoh, T., Kitazawa, M., Shirato, H., Nishizaki, T., 1995. Response characteristics of rain-wind-induced vibration of stay-cables of cable-stayed bridges. Journal of Wind Engineering and Industrial Aerodynamics 57, 323–333.

Matsumoto, M., Daito, Y., Kanamura, T., Shigemura, Y., Sakuma, S., Ishizaki, H., 1998. Wind-induced vibration of cables of cable-stayed bridges. Journal of Wind Engineering and Industrial Aerodynamics 74–76, 1015–1027.

Matsumoto, M., Yagi, T., Goto, M., Sakai, S., 2003. Rain-wind-induced vibration of inclined cables at limited high reduced wind velocity region. Journal of Wind Engineering and Industrial Aerodynamics 91, 1–12.

Naprstek, J., Pospisil, S., Hracov, S., 2007. Analytical and experimental modelling of non-linear aeroelastic effects on prismatic bodies. Journal of Wind Engineering and Industrial Aerodynamics 95, 1315–1328.

Parkinson, G.V., 1989. Phenomena and modelling of flow-induced vibrations of bluff bodies. Progress in Aerospace Science 26 (2), 169–224.

Robertson, A., Taylor, I., Wilson, S., Duffy, B., Sullivan, J., 2010. Numerical simulation of rivulet evolution on a horizontal cable subject to an external aerodynamic field. Journal of Fluids and Structures 26, 50–73.

Verwiebe, C., Rucheweyh, H., 1998. Recent research results concerning the exciting mechanisms of rain-wind-induced vibrations. Journal of Wind Engineering and Industrial Aerodynamics 74–76, 1005–1013.